Available online at www.sciencedirect.com
SCIENCE DIRECT®
European Journal of Mechanics B/Fluids 23 (2004) 571–585

Flow patterns behind the free flow front for a Newtonian fluid injected between two infinite parallel plates

Heike J.J. Gramberg [a,*], Jos C.W. van Vroonhoven [b], Alphons A.F. van de Ven [a]

[a] *Mathematics and Computing Science, Technische Universiteit Eindhoven, 5600 MB Eindhoven, The Netherlands*
[b] *LG. Philips Displays Netherlands B.V., 5600 AV Eindhoven, The Netherlands*

Received 7 March 2003; received in revised form 4 September 2003; accepted 1 December 2003

Available online 7 February 2004

Abstract

A complete analytical treatment of the 2-dimensional problem of the injection of a Newtonian fluid between two parallel plates is presented. Explicit formulas are derived for the shape of the free flow front, the streamlines behind the flow front, the velocity, deformation and rotation (orientation) of material elements in the flow front region, and the associated stresses there. The analysis is based on complex function theory, and in this, the flow region, inclusive the unknown free flow front, is mapped onto the interior of the unit circle. The mapping function that determines the shape of the flow front is found by solving a Hilbert problem. It is analytically found in how far the actual flow front differs from a semi-circular shape, and it is concluded that the semi-circular approximation seems acceptable. Deformations of material line or area elements due to the fountain flow in the flow front region are followed in time; large deformation and reorientations of the material elements are observed. Our results are compared with results in literature obtained by numerical simulations and by experimental work, and on the whole good correspondence is found.

Keywords: Injection moulding; Free flow front; Fountain flow; Molecular orientation; Conformal mapping

1. Introduction

Injection moulding, especially in the filling phase, is a process exhibiting several peculiar but interesting aspects. To name some: the flow has a free boundary, the *flow front*, behind which a *fountain flow* occurs. Induced by this fountain flow, changes of *molecular orientation* in the injected polymer take place. Questions arise such as: what is the shape of the free flow front, how are the streamlines of the fountain flow directed, and how does the flow deform and reorientate a material line element moving to the wall of the mould? More advanced questions are: is the shape of the flow front stationary or does it change ("wobble"), and is this flow always stable? In this paper, we will restrict ourselves to injection moulding between two parallel plates; in this case the mould consists of a narrow striplike (2-dimensional) cavity bounded by two fixed walls.

Many articles have dealt with these subjects. The shape of the flow front was already calculated in the 80ties by [1–3]. Here, Diereck, [1], and Mavridis et al., [2], used finite element computations to calculate the front shape, whereas Vroonhoven and Kuijpers, [3], introduced a completely analytical approach, leading to an explicit formula for the flow front. Recent papers show more advanced numerical techniques; e.g., Friedrichs and Güçeri, [4], applied an hybrid 2-D/3-D numerical technique to compute the flow front, and the fountain flow behind it, for a shear-thinning non-Newtonian fluid. Such a 2-D/3-D approach was also proposed by Almeida et al., [5], by means of a so called Dimensional Reduction Method, based on a minimum

* Corresponding author.
E-mail address: h.j.j.gramberg@tue.nl (H.J.J. Gramberg).

0997-7546/$ – see front matter
doi:10.1016/j.euromechflu.2003.12.003

energy principle. Other authors, such as Nguyen-Chung and Mennig, [6], used front tracking methods, whereas Pichelin and Coupez, [7], used a global transport equation to find the flow front position. In [7, Figs. 6 and 7], flow fronts for a Newtonian and a non-Newtonian, shear-thinning, fluid are compared; no great qualitative differences are found. A visualisation of the flow front behaviour by means of a flow front tracking camera system was recently presented by Yokoi et al., [8]. Results for the streamlines of the fountain flow behind the flow front are incorporated in, e.g., [1,2,10,9]. Mavridis et al., [9], exploiting a Leonov viscoelastic model, also pictured the deformation of a material fluid element behind the flow front; when comparing with earlier results, [2], for a Newtonian fluid, the authors concluded that similar deformation patterns were found. In [6], an interesting figure, depicting the deformation of an initially straight, transverse, material line, can be found.

A paper deserving special interest is the one from Kamal et al., [11], who performed a numerical simulation for a polymer melt. They computed velocity profiles and stresses for two constitutive models: a power-law fluid and a viscoelastic (White–Metzner) model. Comparing the results, they found essentially the same velocity profiles (with only minor quantitative differences in the transverse profile), but significant differences in the stress profiles. The latter did not so much hold for the shear stresses inside the flow front region (see [11, Fig. 7, CP- and (CP+2)-lines]), but the more for the first normal stress difference [11, Fig. 8]. The authors also replace, in order to alleviate the singularities occurring at the separation point, the no-slip condition at the walls by a slip condition in a small region behind the separation point. This modification affects the behaviour near the walls in the vicinity of the separation point essentially; this shows up most evident in the shear stresses (see [11, Fig. 5]).

Molecular orientation, especially with regard to aspects such as residual stresses, birefringence, surface defects, and flow front instabilities, was studied in a series of references, of which we mention here [6,9,12–15]. In his thesis, Wimberger and Friedl, [13], mainly focussed on the effects of the molecular orientation on birefringence. Hung and Shen, [14], calculated the fibre orientation using Jeffery's model for a generalised Newtonian fluid. Vincent et al., [15], looked at the orientation of short fibres in reinforced thermoplastics due to fountain flow. Effects on surface defects and on flow front instabilities are thoroughly investigated by Grillet et al., [16], and by Bogaerds et al., [17,18], respectively.

Except in [3], all the results in the papers listed above are derived by numerical means. For our purposes, we prefer an analytical approach, as in [3], and we want to calculate the shape of the flow front, the velocity field behind the flow front, the induced deformation and reorientation of material line elements, and the resulting stresses, all by *purely analytical means*. In doing this, we shall follow the lines set up by Vroonhoven and Kuijpers, [3]; in particular, in Section 3, we shall shortly recapitulate how they came to their explicit formula for the shape of the flow front. Starting from this result, we then proceed with the calculations of velocities, deformations, and stresses; this was not done explicitly in [3]. Of course, these purely analytical calculations can only be done for a simple case. Therefore, we restrict ourselves to a two-dimensional injection between two parallel plates of an incompressible Newtonian fluid, with a no-slip boundary condition at the walls of the mould. Thermal effects are not taken into account. The shape of the flow front is fixed and moving with constant velocity. Far behind the flow front, the flow is a Poiseuille flow. The analysis is based on the theory of complex functions, [19], and on a conformal mapping of the flow front onto a unit circle. The specific form of this conformal mapping is the principal unknown in this problem. Once the mapping is known, all other quantities can be calculated. It turns out that the shape of the flow front is very close to, but not identically equal to, a semi-circle, as is confirmed by several other articles, [1,2] (see also Table 1), [10,11,17] (see Fig. 5.9).

In Section 4, the results of Section 3 are further evaluated to explicit formulas for especially the velocity in the flow front region. Other kinematical quantities such as deformations and rotations, as well as dynamical ones as stresses, can then be analytically calculated. The results are presented in Section 5, while the main conclusions are listed in Section 6. As far as the kinematical results concern, the behaviour as found here corresponds very well with behaviour found in literature for much more complex fluid models. Therefore, a Newtonian model seems adequate enough to describe in a first order the *kinematics* of fountain flow for polymer melts of general constitutive nature (non-Newtonian, nonlinear viscoelastic).

2. Problem description

A fluid is injected with prescribed volumetric flow rate between two infinite parallel plates at distance $2h$. The flow is 2-dimensional in the X–Y-plane; see Fig. 1. The fixed origin O of an $\{OXY\}$ system is midway between the plates, the X-axis points in the flow direction and the Y-axis is perpendicular to the plates ($-h < Y < h$). In the flow considered here, the flow front Γ_f is an unknown free surface. In the next section, we shall show how the shape of Γ_f can be determined completely by analytical means. For this, we restrict ourselves to an incompressible Newtonian fluid model, in which case a fully analytical solution can be obtained.

We assume the flow so slow, and the viscosity of the fluid so high, that all inertia effects may be neglected (small Reynolds number $\Rightarrow$ Stokes flow). Moreover, the shape of the flow front is taken constant (stationary) and the front moves with constant speed V_f.

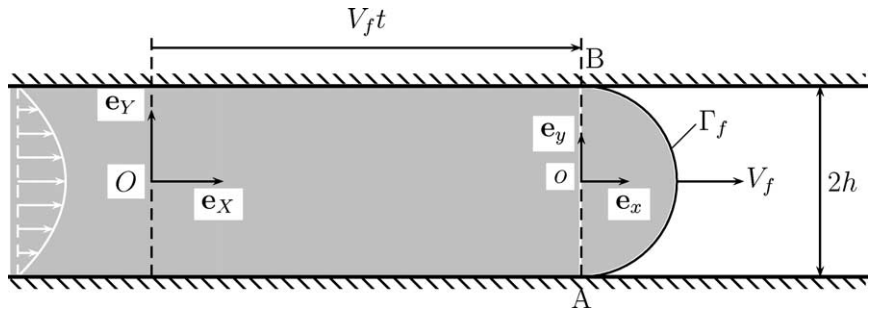

Fig. 1. The flow region with moving front between two plates.

Far behind the flow front,[1] the flow is a fully developed Poiseuille flow. Here, the velocity $\mathbf{V} = U\mathbf{e}_X + V\mathbf{e}_Y$ is given by

$$U = \frac{3}{2}V_f\left[1 - \left(\frac{Y}{h}\right)^2\right], \qquad V = 0. \tag{1}$$

The actual flow front region is given by the area between the line *AB*, see Fig. 1, and the free flow front Γ_f. Note that this area moves with constant speed V_f. Therefore, we introduce a comoving frame $\{oxy\}$, as depicted in Fig. 1, with the dimensionless coordinates

$$x = \frac{X - V_f t}{h}, \quad y = \frac{Y}{h} \quad (-1 < y < 1). \tag{2}$$

In this comoving frame, the flow front is given by

$$\Gamma_f(x, y) = 0, \tag{3}$$

where the function $\Gamma_f(x, y)$ is still to be determined.

The dimensionless velocity $\mathbf{v} = u(x, y)\mathbf{e}_x + v(x, y)\mathbf{e}_y$ with respect to the comoving frame is related to the dimensional absolute velocity $\mathbf{V}(X, Y, t)$ by

$$U = V_f(1 + u), \qquad V = V_f v. \tag{4}$$

The stationary flow of the incompressible Newtonian fluid is governed by the Stokes equation together with the incompressibility condition. This implies that the velocity components u and v are biharmonic functions, which can be expressed in two complex analytical functions.

For the boundary conditions, we have

- at the walls $y = \pm 1$: a no-slip condition, i.e., $\mathbf{V} = \mathbf{0}$, yielding

$$u(x, \pm 1) = -1, \qquad v(x, \pm 1) = 0; \tag{5}$$

- for $x \to -\infty$: fully developed Poiseuille flow, according to (1), yielding

$$u(x, y) \to u_0(y) = \frac{1}{2} - \frac{3}{2}y^2, \qquad v(x, y) \to 0; \tag{6}$$

- at the flow front $(x, y) \in \Gamma_f$, being a free flow front, we require

$$\mathcal{T}\mathbf{n} = -p_0\mathbf{n}, \tag{7}$$

  where $\mathcal{T}$ is the stress tensor, $\mathbf{n}$ is the unit outward normal vector on Γ_f, and p_0 is the environmental pressure;
- finally, we need the free-flow-front condition, stating that the front curve Γ_f must be a flow line. This is expressed by

$$(\mathbf{v}, \mathbf{n}) = 0, \quad \text{for } (x, y) \in \Gamma_f. \tag{8}$$

[1] 'Far behind the flow front' means effectively only a few times h, and more, behind the flow front.

3. Complex formulation and solution

In this section, we only present the main lines for the determination of Γ_f, by means of the theory of complex functions and conformal mapping. For the details of the derivations, we refer to [3].

Following [3] (see also [19], Eq. (2.44), with $\kappa = 1$), we can express the complex velocity $w = u + \mathrm{i}v$ and the stresses in terms of two complex potentials $\Omega(z)$ and $\omega(z)$, as (here, $z = x + \mathrm{i}y$, the complex variable, $'$ means differentiation with respect to z, and $\overline{f(z)}$ denotes the complex conjugate of $f(z)$)

$$\begin{aligned} w(z,\bar{z}) &= z\overline{\Omega'(z)} + \overline{\omega'(z)} - \Omega(z), \\ N(z,\bar{z}) &= T_{xx} + T_{yy} = -2\big(\Omega'(z) + \overline{\Omega'(z)}\big), \\ S(z,\bar{z}) &= T_{xx} - T_{yy} + 2\mathrm{i}T_{xy} = 2z\overline{\Omega''(z)} + 2\overline{\omega''(z)}. \end{aligned} \tag{9}$$

To eliminate the influence of the environmental pressure p_0 and of the flow far behind the flow front ($w \to u_0(y)$ for $\mathrm{Re}(z) \to -\infty$), we write $\Omega(z) = \Omega_0(z) + \Omega_1(z)$ and $\omega(z) = \omega_0(z) + \omega_1(z)$, where

$$\Omega_0(z) = -\frac{1}{4}\left(1 + \frac{3}{2}z^2\right) + \frac{1}{2}p_0 z, \qquad \omega_0(z) = \frac{1}{4}z\left(1 + \frac{1}{2}z^2\right). \tag{10}$$

The boundary conditions (5)–(8) in terms of $\Omega_1(z)$ and $\omega_1(z)$ become:

$$\begin{aligned} &z\overline{\Omega_1'(z)} + \overline{\omega_1'(z)} - \Omega_1(z) = 0, \quad \mathrm{Im}(z) = \pm 1, \\ &z\overline{\Omega_1'(z)} + \overline{\omega_1'(z)} - \Omega_1(z) \to 0, \quad \mathrm{Re}(z) \to -\infty, \\ &z\overline{\Omega_1'(z)} + \overline{\omega_1'(z)} + \Omega_1(z) = \frac{3}{8}\big(z^2 + 2z\bar{z} - \bar{z}^2\big), \quad z \in \Gamma_f, \\ &\mathrm{Re}\Big[\big(z\overline{\Omega_1'(z)} + \overline{\omega_1'(z)} - \Omega_1(z)\big)(n_x - \mathrm{i}n_y)\Big] = \frac{3}{2}\big(\mathrm{Im}(z)\big)^2 - \frac{1}{2}, \quad z \in \Gamma_f. \end{aligned} \tag{11}$$

The basic idea of the method used in [3] is to map the total flow region G_z in the z-plane onto the unit circle G_ζ^+ in the ζ-plane and then to reduce the problem to a so called *Hilbert problem* on the unit circle, that can explicitly be solved in terms of the conformal mapping $m(\zeta)$. In this way, the problem of determining the explicit shape of the flow front is tackled completely by analytical means. The conformal mapping $z = m(\zeta)$, depicted in Fig. 2, is by definition analytic, implying that it can be expressed as an infinite power series, with radius of convergence 1,

$$m(\zeta) = \sum_{k=0}^{\infty} \mu_k \zeta^k, \tag{12}$$

which will be approximated by the truncated series

$$m_N(\zeta) = \sum_{k=0}^{N} \mu_k \zeta^k. \tag{13}$$

Note that, as the shape of Γ_f is unknown, the real coefficients μ_k in (13) are still unknown.

Next, $\Omega_1(z)$ and $\omega_1(z)$ are replaced by functions of ζ by means of the substitution $z = m_N(\zeta)$, yielding

$$\Omega_N(\zeta) = \Omega_1\big(m_N(\zeta)\big), \qquad \omega_N(\zeta) = \omega_1\big(m_N(\zeta)\big), \tag{14}$$

for $\zeta \in G_\zeta^+$.

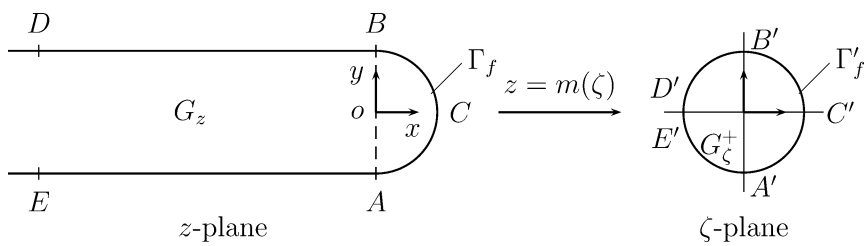

Fig. 2. The conformal mapping of G_z onto the unit circle G_ζ^+.

For the evaluation of the fourth boundary condition of (11), we need the analytical continuation of $\Omega_N(\zeta)$ to the exterior space G_ζ^- of the unit circle, which is denoted by $\Psi_N(\zeta)$. As shown in [3], this leads to the formulation of the following *Hilbert problem* for Ψ_N; see [3, (4.13), (4.14)] (here, $\Psi_N^\pm(\xi) = \lim_{\zeta\to\xi,\ \zeta\in G_\zeta^\pm} \Psi_N(\zeta)$)

$$\begin{aligned} &\Psi_N^+(\xi) - \Psi_N^-(\xi) = 0, \quad \xi \in A'E'D'B', \\ &\Psi_N^+(\xi) + \Psi_N^-(\xi) = g_N(\xi), \quad \xi \in \Gamma_f', \end{aligned} \tag{15}$$

where

$$g_N(\xi) = \frac{3}{8}\big(m_N(\xi)^2 + 2m_N(\xi)\overline{m_N(\xi)} - \overline{m_N^2(\xi)}\big). \tag{16}$$

The solution procedure of (15) is described in detail in [3], where it is shown that the solution can be split up into a particular solution and a homogeneous one, as

$$\Psi_N(\zeta) = X(\zeta)G_N(\zeta) + X(\zeta)F_N(\zeta), \tag{17}$$

where $X(\zeta)$ is the *Plemelj function*:

$$X(\zeta) = (\zeta - \mathrm{i})^{1/2}(\zeta + \mathrm{i})^{1/2}, \quad \zeta \in \mathbb{C} \setminus \Gamma_f', \tag{18}$$

satisfying

$$X^+(\xi) + X^-(\xi) = 0, \quad \xi \in \Gamma_f', \tag{19}$$

while G_N is defined by the *Cauchy integral*,

$$G_N(\zeta) = \frac{1}{2\pi\mathrm{i}} \int_{\Gamma_f'} \frac{g_N(\xi)}{X^+(\xi)(\xi - \zeta)}\,\mathrm{d}\xi, \tag{20}$$

and F_N is a polynomial of degree $N-1$,

$$F_N(\zeta) = \sum_{k=0}^{N-1} f_k \zeta^k, \tag{21}$$

the coefficients of which can be determined by means of the holomorphy condition (see Section 4).

The Plemelj function $X(\zeta)$ has branch points at $\zeta = \pm\mathrm{i}$, and the cut, joining $-\mathrm{i}$ with infinity, is defined in such a way that; see [19],

$$X(\zeta) = -\sqrt{1+\zeta^2}, \quad \zeta \in G_\zeta^+, \qquad X(\zeta) = \sqrt{1+\zeta^2}, \quad \zeta \in G_\zeta^-. \tag{22}$$

As will be shown in Section 4, the function $\Psi_N(\zeta)$ can be explicitly expressed in the coefficients of the conformal mapping $m_N(\zeta)$.

Finally, for the determination of $m_N(\zeta)$ we need the flow-front condition $(\mathbf{v}, \mathbf{n}) = 0$ on Γ_f', as expressed by the fourth boundary condition of (11), which can be evaluated into (compare with [3, (4.8)])

$$\mathrm{Re}\left(\left[\frac{1}{2} - \frac{3}{2}\big(\mathrm{Im}\ m(\xi)\big)^2 + g_N(\xi) - 2\Psi_N^+(\xi)\right]\overline{\xi m_N'(\xi)}\right) = 0, \quad \xi \in \Gamma_f'. \tag{23}$$

What remains now is the calculation of μ_k, $k = 0, 1, \ldots, N$, from (23). The latter step can only be done numerically (however, by a very simple procedure). Results for several values of N are presented by Vroonhoven and Kuijpers in [3]. As an example, for the case $N = 3$ they found

$$\mu_0 = -0.04287, \quad \mu_1 = 0.98349, \quad \mu_2 = -0.04287, \quad \mu_3 = -0.01651. \tag{24}$$

In Fig. 3, the exact flow front is compared with a semi-circle, and a reasonable resemblance is found; a similar result is found in [2, Figs. 13, 14]. Moreover, in all the references cited in Introduction in which a flow front is found (including shear-thinning fluids) the maximal deviation from a semi-circle is between 0 and 10 percent.

In [3], Vroonhoven and Kuijpers presented explicit results only for the shape of the global flow front (it was globally indicated how the velocity can be calculated, once the coefficients μ_k are know, but this was not evaluated there). However, an explicit (analytical) expression for the velocity in the flow front, and the stresses there, is just what we want to find.

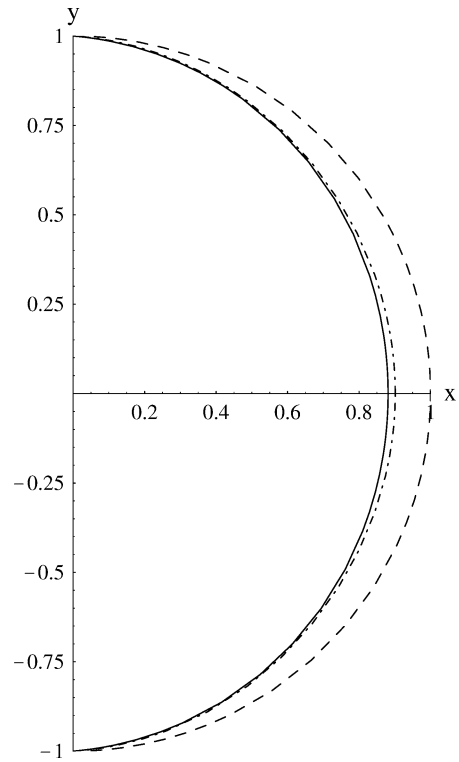

Fig. 3. The flow front for $n = 3$ (full line) and $n = 4$ (dash-dotted line) compared with a semi-circle (dashed line).

In [3], see (4.9) and (4.15), the following expression for the complex velocity $w_n(\zeta)$, for $\zeta \in G^+$, was derived:

$$w_N(\zeta) = \frac{1}{2} - \frac{3}{2}\,\mathrm{Im}\big(m_N(\zeta)\big)^2 + w_{N1}(\zeta), \tag{25}$$

where $w_{N1}(\zeta)$ is given by

$$w_{N1}(\zeta) = \Psi_N(1/\bar{\zeta}) - \Psi_N(\zeta) + \frac{m_N(\zeta) - m_N(1/\bar{\zeta})}{\overline{m'_N(\zeta)}}\,\overline{\Psi'_N(\zeta)}, \tag{26}$$

and $\Psi_N(\zeta)$ is given by (17).

In the next section we shall show that $\Psi_N(\zeta)$ can be determined as

$$\Psi_N(\zeta) = \frac{1}{2}g_N(\zeta) - \frac{1}{2}X(\zeta)\left(\sum_{k=-2N}^{-1} a_k\zeta^k + \sum_{k=0}^{2N-1} b_k\zeta^k - 2\sum_{k=0}^{N-1} f_k\zeta^k\right), \tag{27}$$

for $\zeta \in \mathbb{C} \setminus \Gamma'_f$, where

$$g_N(\zeta) = \frac{3}{8}\big(m_N^2(\zeta) + 2m_N(\zeta)\overline{m_N(1/\bar{\zeta})} - \overline{m_N^2(1/\bar{\zeta})}\big) \tag{28}$$

(note that $g_N(\xi)$ is the limit of $g_N(\zeta)$ for $\zeta \to \xi \in \Gamma'_f$) and a_k and b_k are the coefficients in the Laurent series

$$\begin{aligned} \frac{g_N(\zeta)}{X(\zeta)} &= \sum_{k=-2N}^{\infty} a_k\zeta^k, \quad \zeta \in G^+, \\ \frac{g_N(\zeta)}{X(\zeta)} &= \sum_{k=-\infty}^{2N-1} b_k\zeta^k, \quad \zeta \in G^-. \end{aligned} \tag{29}$$

The coefficients a_k, b_k, and f_k will be calculated in terms of the μ_k's, $k = 0, 1, \ldots, N$, in the next section.

4. Further evaluation of the results of Section 3

As mentioned in the previous section, if N is given and μ_k for $k = 0, \ldots, N$ known, we can determine the coefficients a_k, b_k and f_k analytically. In this section, we will outline the procedure how to do this, and how this will eventually result in an explicit expression for the complex velocity $w_N(\zeta)$.

The coefficients a_k and b_k follow from their definitions, (29), and can be calculated explicitly in terms of μ_k, $\mu_k \in \mathbb{R}$. For this, we start with the analytical function $g_N(\zeta)$ introduced in (28), in which we eliminate $m_N(\zeta)$ by use of (13). Thus, we obtain, for $\zeta \in \mathbb{C}\backslash\{0\}$,

$$g_N(\zeta) = \frac{3}{8}\left(\sum_{i=0}^{2N}\sum_{j=0}^{N} \mu_j \mu_{i-j} \zeta^i + 2 \sum_{i=-N}^{N}\sum_{j=0}^{N} \mu_j \mu_{j-i} \zeta^i - \sum_{i=-2N}^{0}\sum_{j=0}^{N} \mu_j \mu_{-j-i} \zeta^i \right), \tag{30}$$

where we define $\mu_i = 0$ for $i < 0$ or $i > N$.

Developing $1/X(\zeta)$ for $\zeta \in G_\zeta^+$ (with use of (22)) into powers of ζ, combining this with (30), and using this in the definition of a_k, (29), we obtain

$$a_k = \sum_{i=0}^{2N} \lambda_{k-i} \sum_{j=0}^{N} \mu_j \mu_{i-j} + 2 \sum_{i=-N}^{N} \lambda_{k-i} \sum_{j=0}^{N} \mu_j \mu_{j-i} - \sum_{i=-2N}^{0} \lambda_{k-i} \sum_{j=0}^{N} \mu_j \mu_{-i-j}, \tag{31}$$

for $k \geqslant -2N$, with λ_j equal to

$$\lambda_j := \begin{cases} -\dfrac{3}{8}\dbinom{-1/2}{k}, & \text{for } j = 2k,\ k \in \mathbb{N} \cup \{0\}, \\ 0, & \text{for } j \text{ odd or } j < 0, \end{cases} \tag{32}$$

where $\binom{-1/2}{k}$ is defined according to

$$\binom{-1/2}{k} = \frac{(-1)^k}{4^k} \frac{(2k)!}{(k!)^2}, \quad k \in \mathbb{N} \cup \{0\}. \tag{33}$$

Analogously, we can develop $g_N(\zeta)$ and $X(\zeta)$ as Taylor series for $\zeta \in G_\zeta^-$, rendering the following equation for b_k

$$b_k = \sum_{i=-2N}^{0} \gamma_{-k-i} \sum_{j=0}^{N} \mu_j \mu_{-i-j} + 2 \sum_{i=-N}^{N} \gamma_{-k-i} \sum_{j=0}^{N} \mu_j \mu_{i+j} - \sum_{i=0}^{2N} \gamma_{-k-i} \sum_{j=0}^{N} \mu_j \mu_{i-j}, \tag{34}$$

where $k < 2N - 1$, and γ_j is given by

$$\gamma_j := \begin{cases} \dfrac{3}{8}\dbinom{-1/2}{k}, & \text{for } j = 2k+1,\ k \in \mathbb{N} \cup \{0\}, \\ 0, & \text{for } j \text{ even or } j < 0. \end{cases} \tag{35}$$

In order to calculate f_k, we first need to find an explicit expression for $G_N(\zeta)$ in terms of a_k, b_k and g_N. Consider the following integrals

$$\begin{aligned} I_1(\sigma) &:= \frac{1}{2\pi \mathrm{i}} \int_L \frac{g_N(\zeta)}{X(\zeta)(\zeta - \sigma)} \,\mathrm{d}\zeta, \\ I_2(\sigma) &:= \frac{1}{2\pi \mathrm{i}} \int_{C_R} \frac{g_N(\zeta)}{X(\zeta)(\zeta - \sigma)} \,\mathrm{d}\zeta, \end{aligned} \tag{36}$$

where L is a contour enclosing Γ_f', but such that the points 0 and σ lie outside L, while C_R is a circle with radius $R > \max\{1, |\sigma|\}$ as depicted in Fig. 4. By taking into account that

$$\frac{g_N(\zeta)}{X(\zeta)(\zeta - \sigma)} = \mathrm{O}\big(\delta^{-1/2}\big), \quad \text{for } |\zeta \pm \mathrm{i}| =: \delta \to 0, \tag{37}$$

and by using (19) and (20), we find the following expression for $I_1(\sigma)$

$$I_1(\sigma) = \frac{1}{2\pi \mathrm{i}} \int_{\Gamma_f'} \frac{g_N(\xi)}{X^+(\xi)(\xi - \sigma)} \,\mathrm{d}\xi - \frac{1}{2\pi \mathrm{i}} \int_{\Gamma_f'} \frac{g_N(\xi)}{X^-(\xi)(\xi - \sigma)} \,\mathrm{d}\xi = 2G_N(\sigma). \tag{38}$$

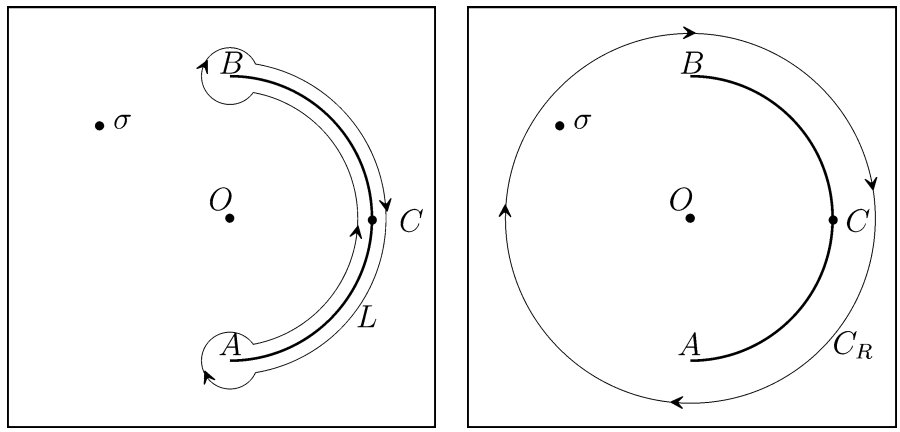

Fig. 4. Contours L and C_R.

Since $g_N(\zeta)/X(\zeta)$ is holomorphic outside C_R and σ is a point inside C_R, the integral $I_2(\sigma)$ is equal to the residue of the integrand in infinity (see [19, Eq. (1.15)]) and thus we find the following expression for $I_2(\sigma)$, with use of (29),

$$I_2(\sigma) = -\sum_{k=0}^{2N-1} b_k \sigma^k. \tag{39}$$

From the residue theorem of Cauchy, it follows that

$$I_1(\sigma) - I_2(\sigma) = \mathrm{Res}_{\zeta=\sigma} \frac{g_N(\sigma)}{X(\zeta)(\zeta-\sigma)} + \mathrm{Res}_{\zeta=0} \frac{g_N(\sigma)}{X(\zeta)(\zeta-\sigma)} = \frac{g_N(\sigma)}{X(\sigma)} - \sum_{k=-2N}^{-1} a_k \sigma^k. \tag{40}$$

Combining (38)–(40), we find the following expression for $G_N(\zeta)$, valid in $\mathbb{C}\backslash\{\Gamma_f'\}$,

$$2G_N(\zeta) = \frac{g_N(\zeta)}{X(\zeta)} - \sum_{k=-2N}^{-1} a_k \zeta^k - \sum_{k=0}^{2N-1} b_k \zeta^k. \tag{41}$$

From the first equation of (29), we see that the singularity in $\zeta = 0$ is removable. For $|\zeta| \to \infty$, the second equation of (29) yields

$$2G_N(\zeta) = \sum_{k=-\infty}^{2N-1} b_k \zeta^k - \sum_{-2N}^{-1} a_k \zeta^k - \sum_{k=0}^{2N-1} b_k \zeta^k = \mathrm{O}\left(\frac{1}{\zeta}\right). \tag{42}$$

So, the function G_N is holomorphic in $\mathbb{C}\backslash\{\Gamma_f'\}$, including the point at infinity. We proceed with the calculation of the polynomial $F_N(\zeta)$ by considering the holomorphy condition, expressing that the analytical function $\omega_N'(\zeta)$ must remain finite for $\zeta \to 0$. According to [3, (5.12)] this condition reads (for convenience, we have divided the condition of [3] by $X(\zeta)$, which is allowed because $X(0)$ is bounded; $X(0) = -1$)

$$-\frac{\omega_N'(\zeta)}{X(\zeta)} = -\frac{m_N'(\zeta)\overline{\Psi_N(1/\bar{\zeta})}}{X(\zeta)} + \frac{\overline{m_N(1/\bar{\zeta})}\Psi_N'(\zeta)}{X(\zeta)} = \mathrm{O}(1), \quad \text{for } \zeta \to 0. \tag{43}$$

Since (see (22))

$$\overline{X(1/\bar{\zeta})} = -\frac{1}{\zeta} X(\zeta), \tag{44}$$

we obtain from (17) with the aid of (42), for $\zeta \to 0$,

$$\frac{\overline{\Psi_N(1/\bar{\zeta})}}{X(\zeta)} = -\frac{1}{\zeta}\left(\overline{G_N(1/\bar{\zeta})} + \overline{F_N(1/\bar{\zeta})}\right) = -\frac{1}{\zeta}\overline{F_N(1/\bar{\zeta})} + \mathrm{O}(1), \tag{45}$$

according to (42).

Moreover,

$$X'(\zeta) = \frac{\zeta}{\zeta^2+1} X(\zeta), \tag{46}$$

from which it follows that

$$\frac{\Psi_N'(\zeta)}{X(\zeta)} = \frac{\mathrm{d}}{\mathrm{d}\zeta}\left(\frac{\Psi_N(\zeta)}{X(\zeta)}\right) + \frac{\zeta}{\zeta^2+1}\frac{\Psi_N(\zeta)}{X(\zeta)} = G_N'(\zeta) + F_N'(\zeta) + \frac{\zeta}{\zeta^2+1}\big(G_N(\zeta)+F_N(\zeta)\big). \tag{47}$$

For $\zeta \in G_\zeta^+$, we may approximate $G_N(\zeta)$ by means of a Taylor series development around the point $\zeta = 0$, according to

$$G_N(\zeta) = \sum_{j=0}^{\infty} g_j \zeta^j, \tag{48}$$

where g_j follows from (41), with use of (29), as

$$g_j = \begin{cases} \dfrac{1}{2}(a_j - b_j), & \text{for } 0 \leqslant j < 2N, \\ \dfrac{1}{2}a_j, & \text{for } j \geqslant 2N. \end{cases} \tag{49}$$

Substitution of (13) and (45)–(49) into (43) renders the following asymptotic expansion for $\omega_N'(\zeta)/X(\zeta)$, for $\zeta \to 0$,

$$\begin{aligned} -\frac{\omega_N'(\zeta)}{X(\zeta)} = {} & \zeta^{-N}\sum_{i=0}^{N-1}\left(\sum_{j=0}^{i}(j+1)\mu_{j+1}f_{N-1-i+j}\right)\zeta^i + \zeta^{-N}\sum_{i=0}^{N-1}\left(\sum_{j=0}^{i}(j+1)\mu_{N-i+j}(g_{j+1}+f_{j+1})\right)\zeta^i \\ & + \zeta^{-N}\sum_{i=1}^{N-1}\left(\sum_{j=0}^{i-1}\mu_{N+1-i+j}\sum_{l=0}^{j}\beta_l(g_{j-l}+f_{j-l})\right)\zeta^i + \mathrm{O}(1), \end{aligned} \tag{50}$$

with

$$\beta_j := \begin{cases} (-1)^n, & \text{for } j = 2n, \text{ and } n \in \mathbb{N}\cup\{0\}, \\ 0, & \text{for } j \text{ odd or } j < 0, \end{cases} \tag{51}$$

and where f_N is to be taken equal to zero. The requirement that the right-hand side of (50) must be finite for $\zeta \to 0$, leads us to the following set of linear equations, from which f_k, $0 \leqslant k \leqslant N-1$, can be calculated in terms of μ_k and g_k,

$$\begin{aligned} & \sum_{j=0}^{i}(j+1)\big(\mu_{j+1}f_{N-1-i+j} + \mu_{N-i+j}(g_{j+1}+f_{j+1})\big) \\ & \quad + \sum_{j=0}^{i-1}\mu_{N+1-i+j}\sum_{l=0}^{j}\beta_l(g_{j-l}+f_{j-l}) = 0, \quad \text{for } 0 \leqslant i \leqslant N-1, \end{aligned} \tag{52}$$

where $f_N = 0$.

Now that we have found a_k, b_k, and f_k, in terms of μ_k, we can use this in (27), to obtain an expression for $\Psi_N(\zeta)$, after which we can calculate the complex velocity w_N from (25) and (26) in any point in the flow front area, where a fountain flow is observed. In the next section, this will be made explicit with numerical results for the velocity components for the approximated case: $m_N(\zeta) = \zeta$, that is in case the flow front is approximated by a semi-circle.

4.1. Results for a circular flow front approximation

We will now calculate explicit numerical values for the velocity inside the flow area, close to the flow front region. However, we will do this only within an approximation, in which we approximate the flow front by a semi-circle, meaning that we use $z = m(\zeta) = \zeta$. Although results of [3] show that $\mu_1 \approx 1$ and dominant over the other coefficients μ_k (see for instance (24)), this is certainly not exactly true. However, as we are especially interested in the flow behaviour close to the flow front, where this approximation is best, this seems to us an acceptable approach. We could just as well have used the, more exact, results for $N = 3$ as given in (24), and in fact for a part we did so, but not only were the calculations more complex then, the relevant results were nearly the same (differences less then a few percent).

Therefore, we stick to this approximation, for which we have $N = 1$ and $\mu_0 = 0$ and $\mu_1 = 1$. This implies that in (27), we only need to know the coefficients a_{-2}, a_{-1}, b_0, b_1, and f_0. From (31), (34), and (52), we obtain

$$a_{-2} = b_1 = 2f_0 = \frac{3}{8}, \qquad a_{-1} = b_0 = 0. \tag{53}$$

For $g(\zeta)$ (we omit the index N $(= 1)$ from now on) we obtain from (28)

$$g(\zeta) = \frac{3}{8}\left(\zeta^2 + 2 - \zeta^{-2}\right), \tag{54}$$

and all this leads us with (27) to the following expression for $\Psi(\zeta)$

$$\Psi(\zeta) = \frac{3}{16}\left[\zeta^2 + 2 - \zeta^{-2} \pm \sqrt{1+\zeta^2}\left(\zeta^{-2} - 1 + \zeta\right)\right], \quad \zeta \in \mathbb{C} \setminus \Gamma_f', \tag{55}$$

where the $+$ sign holds for $\zeta \in G_\zeta^+$ and the $-$ sign for $\zeta \in G_\zeta^-$.

This means that for $\zeta \in G_\zeta^+$, when $1/\bar{\zeta} \in G_\zeta^-$,

$$\Psi\left(\frac{1}{\bar{\zeta}}\right) = \frac{3}{16}\left[\bar{\zeta}^{-2} + 2 - \bar{\zeta}^2 - \sqrt{1+\bar{\zeta}^2}\left(\bar{\zeta} - \bar{\zeta}^{-1} + \bar{\zeta}^{-2}\right)\right]. \tag{56}$$

From (25) and (26) and with $m(\zeta) = \zeta = z$, the following expression for the total complex velocity $w(\zeta) = w(z)$ in the flow front region, $z \in G_\zeta^+$, follows

$$w(z) = \frac{1}{2} + \frac{3}{8}(z - \bar{z})^2 - \Psi(z) + \Psi\left(\frac{1}{\bar{z}}\right) + \left(z - \frac{1}{\bar{z}}\right)\overline{\Psi'(z)}. \tag{57}$$

The use of (55) and (56) in (57) results in an explicit, completely analytical, expression for $w(z)$ in terms of $z = x + \mathrm{i}y$ and $\bar{z}$. This expression will be used in the next section to calculate the velocity field of the fountain flow in the flow front region.

5. Velocity field, deformation and rotation, and stresses behind the flow front

The results of Section 4 will be used here to calculate the velocity field in and behind the flow front region. The thus calculated velocity is an approximation of the actual velocity in the fluid, only accurate in the flow front region ($\mathrm{Re}(z) > 0$). Some distance (a few times h) behind the flow front region, we assume the flow to be a Poiseuille flow. In Fig. 5(a), the velocity profiles at the border of the flow front region, i.e., at $\mathrm{Re}(z) = 0$, according to (57) are compared to a fully developed Poiseuille flow. This figure shows that the differences there are already small (less than 10%).

Typical streamline patterns are depicted in Fig. 5(b), showing the streamlines relative to the flow front; this figure clearly demonstrates the fountain flow effect. We note that these streamlines are calculated by the method presented in Section 4, but not for the circular flow front approximation $\mu_1 = 1$, but for the μ-values according to (24). Comparing these results with results found by numerical means in, e.g., [1], [2, Fig. 8], [9], and [10, Fig. 4], a practically complete correspondence is found. In [2], see Figs. 13, 14, the numerically simulated shape of the flow front shows a close resemblance to a semi-circle, in correspondence to our Fig. 3. This motivated our choice made in Section 4 to approximate the flow front by a semi-circle. Moreover, it is noticeable that no qualitative differences are found in [2] between the numerical simulations for Newtonian and for shear-thinning fluids.

In analogy with [9,6], we have analysed the behaviour (deformation, rotation) of material, line or surface, elements in injection flow. In Figs. 6 and 7, we show the behaviour of a rectangular material element entering the fountain flow region. In the first figure, the behaviour relative to the flow front (i.e., in a co-moving frame) is illustrated, while the same behaviour, but now in an inertial frame, is presented in the second figure. We observe how the element is stretched, spills over when reaching the flow front, and becomes very strongly stretched at the wall. Further we notice in Fig. 7 that the tail of the stretched element remains normal to the wall up to the very last moment of reaching the fixed wall.

Following [6], we also looked at the deformation of an initially straight transverse line; the result is depicted in Fig. 8. The latter figure shows striking alikeness with Fig. 5 in [6], obtained from finite elements calculations for a Carreau fluid. Watch especially the typical V-shapes near the wall in the last picture. Finally, we show the behaviour of a material element consisting of two material line elements, initially forming a right angle in Fig. 9. We see that the right angle is folded to a small sharp angle. Moreover, following the element initially orientated in the axial direction, we once more notice that this line element is orientated almost normal to the wall when approaching this wall, and only when it is very near to the wall it suddenly flips over to an orientation parallel to the wall. In practice, the polymer melt solidifies at the cooled walls immediately after injection, forming solid (glass) layers at the walls. This means that the polymer chains that are initially in axial direction, will be frozen

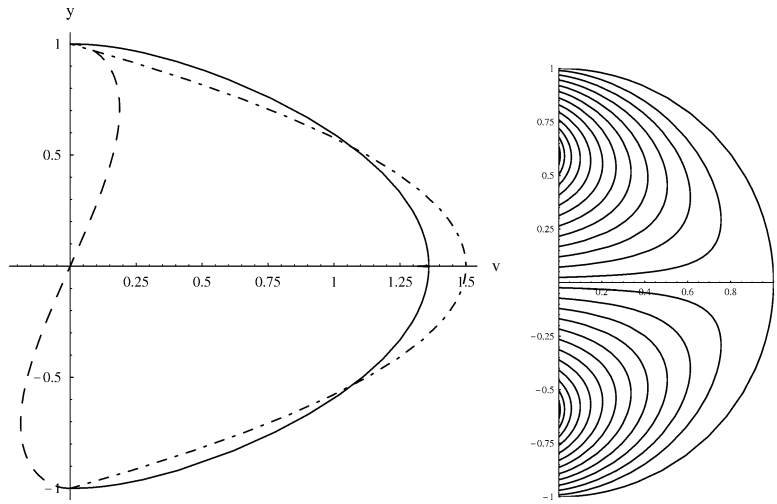

(a) (b)

Fig. 5. (a) The velocity components at the border $x = 0$ of the flow front region (axial velocity u: full line; transverse velocity v: dashed line) compared with the axial velocity in Poiseuille flow (dot-dashed line); (b) Streamlines in co-moving frame.

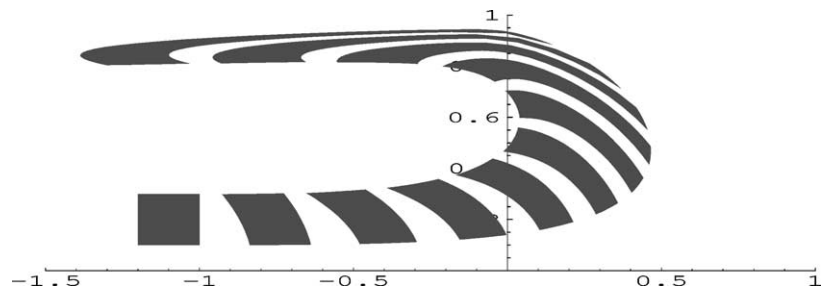

Fig. 6. Behaviour in time of an initially rectangular area element when passing through the flow front region, relative to the flow front.

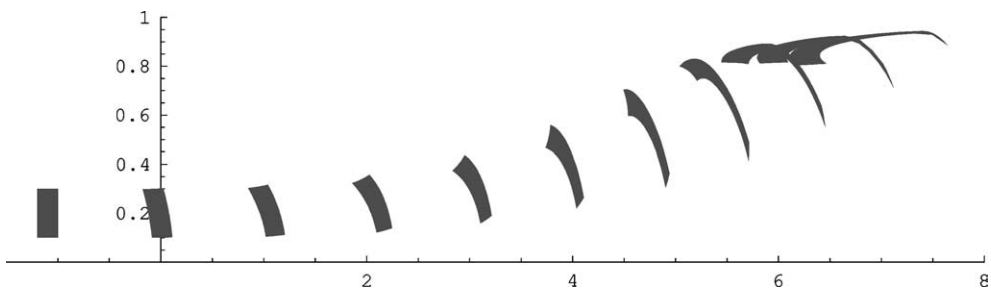

Fig. 7. Behaviour in time of an initially rectangular area element when passing through the flow front region, with respect to the inertial coordinate system.

in having an orientation perpendicular to the walls. This has an essential effect on the frozen-in stresses, and then also on the birefringence, near the walls. This effect is confirmed by numerical simulations and experimental observations, see, e.g., [13, Section 5.1].

The stresses in the fluid, especially in the flow front region, can be calculated from (9). For the stresses, we are interested in the following aspects:

(1) The pressure p, given by

$$p = -\frac{1}{2}(T_{xx} + T_{yy}) = -\frac{1}{2}N(z, \bar{z}) = \Omega_1'(z) + \overline{\Omega_1'(z)} - \frac{3}{4}(z + \bar{z}) = p(x, y). \tag{58}$$

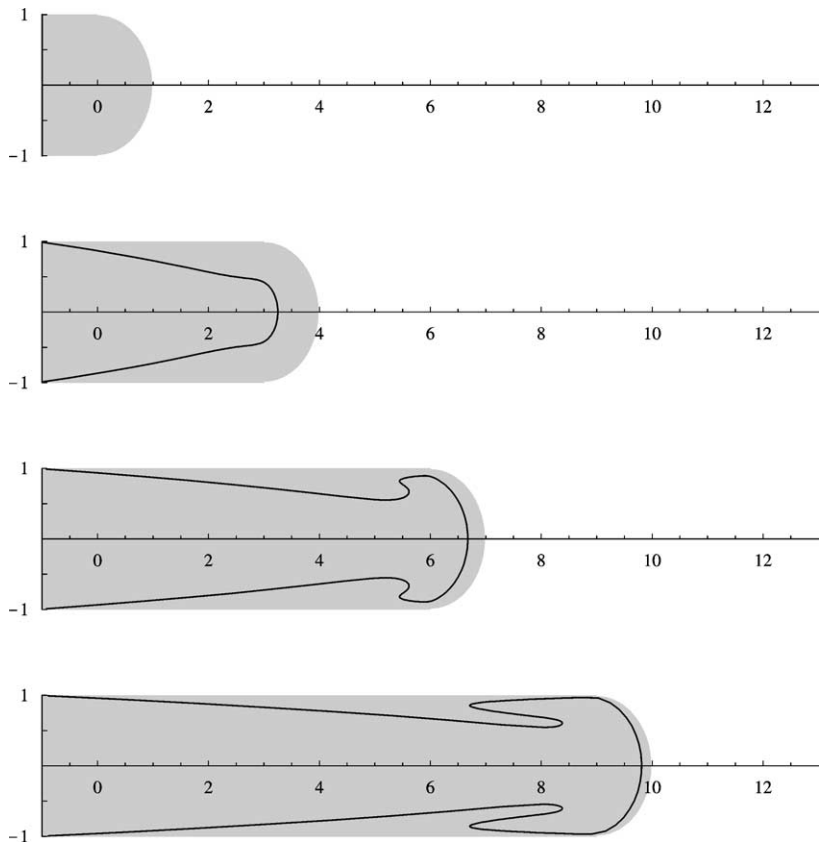

Fig. 8. Deformation of an initially straight transverse line element at four increasing times.

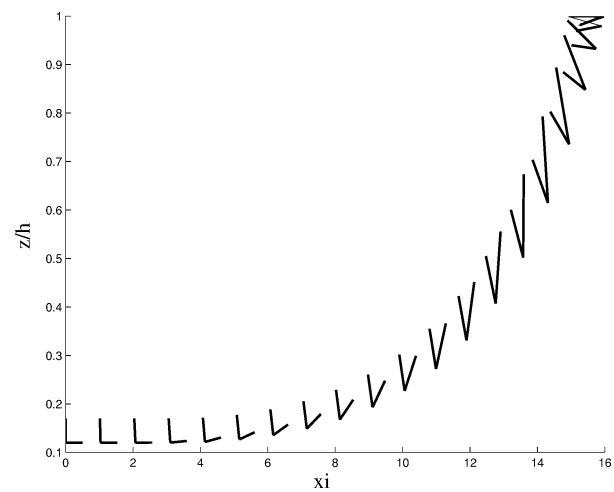

Fig. 9. Transformation of a material element consisting of two line elements, initially forming a right angle.

We have plotted p along the upper wall ($y = 1,\ x < 0$) and the upper part of the flow front Γ_f ($x^2 + y^2 = 1,\ x > 0,\ y > 0$) in Fig. 10. This graph shows a singularity in the point $(x, y) = (0, 1)$. Our analysis predicts that this singularity has an order of $-1/2$ (a square root singularity); this can be inferred from the behaviour of Ψ', and more specifically from that of the Plemelj function in it, for $z \to \pm\mathrm{i}$. The result found here is in good correspondence with that found in [2, Fig. 11] for shear-thinning fluids.

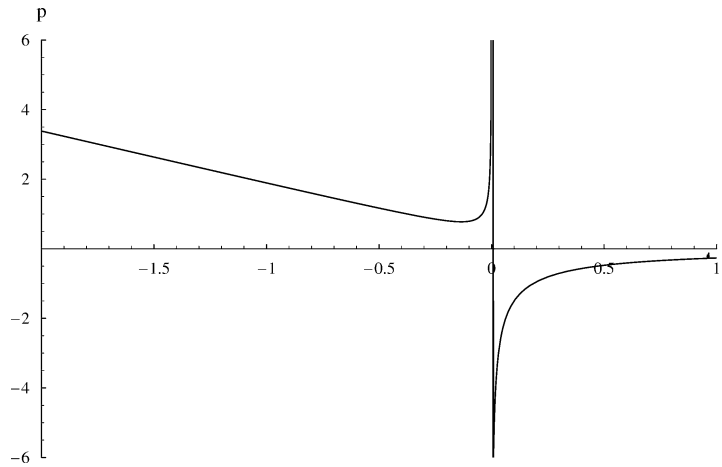

Fig. 10. Pressure along the upper wall and the upper part of the flow front.

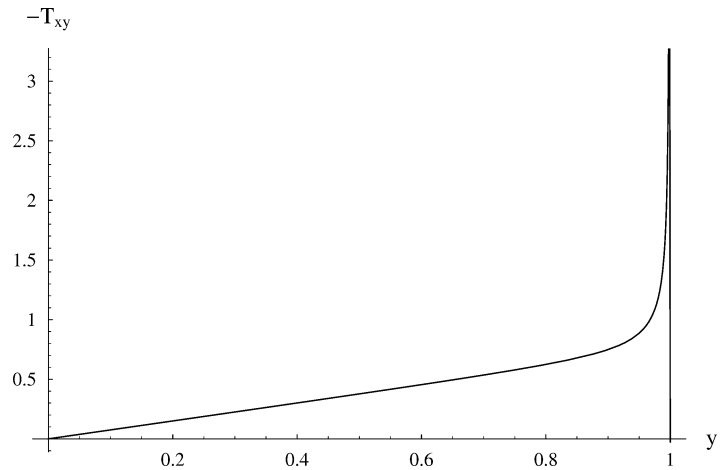

Fig. 11. Shear stress T_{xy} along the border line $x = 0$.

(2) The first normal stress difference N_1, can be found from

$$N_1 = T_{xx} - T_{yy} = \operatorname{Re} S(z, \bar{z}) = z\overline{\Omega_1''(z)} + \bar{z}\Omega_1''(z) + \overline{\omega_1''(z)} + \omega_1''(z) = N_1(x, y). \tag{59}$$

However, we did not depict the results, because we do not expect that our Newtonian model will give a realistic picture of this normal stress difference due to the strong stretches observed in the flow front region. These large elongations can only rightly be incorporated by a nonlinear viscoelastic model, that accounts for the highly elastic influence on the (normal) stresses caused by these elongations.

(3) The shear stress T_{xy}, given by

$$T_{xy} = \frac{1}{2} \operatorname{Im} S(z, \bar{z}) = \frac{1}{2}\left(z\overline{\Omega_1''(z)} - \bar{z}\Omega_1''(z) + \overline{\omega_1''(z)} - \omega_1''(z) - \frac{3}{4\mathrm{i}}(z - \bar{z}) \right). \tag{60}$$

In Fig. 11, the shear stress along the border $x = 0$ of the flow front region is plotted as a function of y for $0 < y < 1$. We see almost linear behaviour on the main part of this line; only in the end point near $y = 1$ a very steep behaviour representing the square root singularity in the stress at the separation point $x = 0$, $y = 1$ is observed. This behaviour is characteristic for Newtonian fluids, when a no-slip condition is maintained (compare for instance with [11, Fig. 5]).

6. Conclusions

A complete analytical model has been developed for the injection moulding of a Newtonian fluid between two parallel plates. Explicit formulas have been derived for the shape of the free flow front (a free-boundary problem) and for the description of the fountain flow in the flow front region. These analytical results were derived by using complex function theory, inclusive a conformal mapping of the flow front onto a circle. The problem was reformulated in terms of a Hilbert problem, that could be solved by means of Plemelj functions. These Plemelj functions are characteristic for the singularities in the separation point, where the fluid separates from the fixed wall. A square root singularity in the stresses is found there. For a global characterization of the flow, the approximation of the actual flow front by a semi-circle is appropriate; this seems to hold irrespective of the rheology of the fluid. It was found that the velocity distribution at the border of the flow front region was very close to that of the Poiseuille flow. This supports the expectation that the flow will be a fully developed Poiseuille flow already a few times (2 or 3) the thickness h behind the flow front. For the region behind the flow front, the full formula for $m(\zeta)$ according to (13) and (24) must be used; thus obtained results (not published in this paper) confirm the expectation mentioned above. We have performed a few calculations using the full formula for $m(\zeta)$, e.g., for calculating the flow patterns within the flow front region; only minor differences with the results published here for $m(\zeta) = \zeta$ are found.

Comparison with existing literature reveals that our theoretical/analytical results show on the whole very good correspondence with numerical and experimental results reported in literature, both qualitative and, whenever possible, quantitative. Kinematical results, such as flow-front shape, velocities, and deformations and rotations (orientation), seem to be quite insensitive to the rheology of the fluid. Of course, this does not hold for the stresses, especially for the normal stress differences, which are very sensitive to elastic effects. These elastic effects become dominant whenever large elongations occur, as in the fountain flow in the flow front region. Moreover, this insensitivity is only present for regular flows; in instability investigations, see [17,18], the specific rheology becomes crucial. Nevertheless, for the unperturbed flow, the rheology is far less relevant.

As our results are purely analytical, they can be incorporated in further research to typical aspects of the free flow front motion in injection moulding. To mention two examples, the flow patterns found here can be used:

- As input for the convection–diffusion temperature problem that is related to the injection moulding of a hot polymer melt into a cold mould. This problem, and specifically the thermal boundaries that show up in it, will be the subject of the forthcoming paper [20]; see also [21].
- As an unperturbed solution for stability problems investigating the (in)stability of slightly perturbed flow front motions ("wobbling of the flow front"). When incorporating also thermal effects by means of [20], the influence of temperature on, e.g., viscosity, and after that the influence of all this on the free motion of the flow front, the effect of an initial asymmetric perturbation on the motion of the front can be analysed; see [21,22]. The instability of the flow front motion is an important problem in the practice of injection moulding, as it causes surface defects on the final product; see [16–18].

References

[1] C. Diereck, Stream function formulation of Stokes problems with stress boundary conditions, Report R479, Philips Research Laboratory, Brussels, 1984.
[2] H. Mavridis, A.N. Hrymak, J. Vlachopolous, Finite element simulation of fountain flow in injection moulding, Polym. Engrg. Sci. 26 (1986) 449–454.
[3] J.C.W. van Vroonhoven, W.J.J. Kuijpers, A free boundary problem for viscous fluid flow in injection moulding, J. Engrg. Math. 24 (1990) 151–165.
[4] B. Friedrichs, S.I. Güçeri, A novel hybrid numerical technique to model 3-D fountain flow in injection moulding process, J. Non-Newtonian Fluid Mech. 49 (1993) 141–173.
[5] A. Almeida, L. Faria, R. Febra, Refined two-dimensional models for the analysis of free boundary flows between parallel plates, Comput. Methods Appl. Mech. Engrg. 151 (1998) 163–180.
[6] T. Nguyen-Chung, G. Mennig, Non-isothermal transient flow and Molecular orientation during injection mold filling, Rheol. Acta 40 (2001) 67–73.
[7] E. Pichelin, T. Coupez, Finite element solution of the 3D mold filling problem for viscous incompressible fluid, Comput. Methods Appl. Mech. Engrg. 163 (1998) 359–371.
[8] H. Yokoi, N. Masuda, H. Mitsuhata, Visualisation analysis of flow front behavior during filling process of injection mold cavity by two-axis tracking system, J. Mat. Proc. Techn. 130–131 (2002) 328–333.
[9] H. Mavridis, A.N. Hrymak, J. Vlachopolous, The effect of fountain flow on molecular orientation in injection moulding, J. Rheol. 32 (1988) 639–663.
[10] T. Sato, S.M. Richardson, Numerical simulation of fountain flow problem for viscoelastic liquids, Polym. Engrg. Sci. 35 (1995) 805–812.

[11] M.R. Kamal, S.K. Goyal, E. Chu, Simulation of injection mold filling of viscoelastic polymer with fountain flow, AIChE J. 34 (1988) 94–106.
[12] Z. Tadmor, Molecular orientation in injection moulding, J. Appl. Polym. Sci. 18 (1974) 1753–1772.
[13] R. Wimberger-Friedl, Orientation, Stress and Density Distributions in Injection-Moulded Amorphous Polymers Determined by Optical Techniques, Ph.D. Thesis, Eindhoven University of Technology, Eindhoven, The Netherlands, 1991.
[14] C.F. Hung, Y.K. Shen, Numerical simulation of fiber orientation in injection mold filling, Int. Comm. Heat Mass Transfer 22 (1995) 791–802.
[15] G. Vincent, E. Devilers, J.F. Agassant, Fibre orientation calculation in injection moulding of reinforced thermoplastics, J. Non-Newtonian Fluid Mech. 73 (1997) 317–326.
[16] A.M. Grillet, A.C.B. Bogaerds, G.W.M. Peters, F.P.T. Baaijens, M. Bulters, Numerical analysis of flow mark surface defects in injection molding flow, J. Rheol. 46 (2002) 651–669.
[17] A.C.B. Bogaerds, Stability analysis of viscoelastic flows, Ph.D. Thesis, Eindhoven University of Technology, Eindhoven, The Netherlands, 2002.
[18] A.C.B Bogaerds, M.A. Hulsen, G.W.M. Peters, F.P.T. Baaijens, Stability analysis of injection molding flows, J. Rheol., submitted for publication.
[19] A.H. England, Complex Variable Methods in Elasticity, Wiley, London, 1971.
[20] H.J.J. Gramberg, A.A.F. van de Ven, Temperature distribution in a Newtonian fluid injected between two semi-infinite plates, in press.
[21] H.J.J. Gramberg, A.A.F. van de Ven, Thermally induced flow front instabilities in injection moulding, in: A.M. Anile, V. Capasso, A. Greco (Eds.), Progress in Industrial Mathematics at ECMI 2000, Springer, Berlin, 2002.
[22] A.A.F. van de Ven, Modelling of industrial processes for polymer melts: Extrusion and injection moulding, in: V. Capasso (Ed.), Mathematical Modelling for Polymer Processing. Polymerization, Cristallization, Manufacture, Springer, Berlin, 2002, pp. 263–309.